Comparison of Structured and Unstructured Grids On Generic Helicopter Fuselage with a Rotor

Choongmo Yang, Takashi Aoyama, Shigeru Saito, JAXA, Japan
Hwajin Nam, Ohjoon Kwon, KAIST, Korea

1. INTRODUCTION

Helicopters are used in various fields such as EMS (Emergency Medical Service), fire fighting, disaster relief, news report, and so on because of the capabilities of hovering and VTOL. However, noise, cost, and VFR (Vision Flight Rules) problems prevent helicopters from being widely used as a means of inter-city transportation in densely populated area.

Prediction of the flow field of helicopter rotors in forward flight is regarded as one of the most challenging problems in current computational fluid dynamics. Addition of the fuselage underneath the rotor further amplifies the complexity, requiring the solution of unsteady three-dimensional flows involving multiple bodies in relative motion. The periodic airloads, which is principally due to the rotating main rotor blades, impact the undesirable noise and vibration on the fuselage in the way of a mutual aerodynamic interference. Therefore, elaborate aerodynamic analyses of the rotor-fuselage interaction are needed to understand the physics and as an aid to the designers.

In the preset study, three dimensional parallel Euler flow solvers have been developed for the simulation of unsteady rotor-fuselage interaction aerodynamics on both structured and unstructured grids using the ROBIN (ROtor Body INteraction) configuration[1-3]. Validations with experimental data are conducted by simulating the flows around the ROBIN fuselage. The merit/demerit of each grid system is discussed.

2. NUMERICAL METHOD

2.1 Numerical Method for Structured Grid

A three-dimensional numerical flow solver for the compressible Euler equation is used to analyze the detailed behavior of tip vortex.

For the calculation of blade grid, inviscid flux vectors are separated using Roe's flux difference splitting (FDS) algorithm[4], with third-order accuracy using a TVD scheme. For the time integration, second-order Euler backward scheme is used in the conventional delta form. A diagonalized ADI method with an upwind flux-split technique is used in the linearized implicit part for the discretionary governing equations. A detailed derivation of the governing equation and numerical schemes is described in a previous work by Aoyama et al.[5] The typical dividing number along the azimuthal direction is about 4800 per revolution, which corresponds to the azimuthal angle about 0.075°. The unsteady calculation is impulsively started from 0°azimuth angle.

For the calculations over background grid, the flux difference across cell interface is divided also using a compact TVD scheme[6] to get third order accuracy. MUSCL cell interface value is modified to achieve 4th-order high accuracy in the background Cartesian grid. Simple High-resolution Upwind Scheme (SHUS)[7] is employed to obtain numerical flux. SHUS is one of the Advection Upstream Splitting Method (AUSM) type approximate Riemann solvers and has small numerical diffusion. The four stage Runge-Kutta method is used for the present calculation. The free stream condition is applied for the outer boundary of the outer background grid.

Calculations are performed using Central Numerical Simulation System (CeNSS), the main part of the third-generation numerical simulator of JAXA. It is composed of high performance UNIX servers, FUJITSU PRIMEPOWERs, which are connected by a crossbar network. CeNSS has 9TFLOPS peak performance, 3TB memory, 50TB disk storage, and 600TB tape archive.

2.2 Numerical Method for Unstructured Grid

The governing unsteady Euler equations are discretized by using a finite-volume method on the inertial coordinate system. The inviscid flux across each cell face is computed based on the Roe's flux difference splitting formula[4]. To obtain second-order spatial accuracy, estimation of the state variables at each cell face is achieved by interpolating the solution using the Taylor series expansion in the neighborhood of each cell center. The cell-averaged solution gradient required at the cell center for the above expansion is computed from the Gauss' theorem by evaluating the surface integral for the closed surface of the tetrahedron. The expansion also requires the nodal value of the solution, which can be computed from the surrounding cell center data using a second-order accurate pseudo-Laplacian averaging procedure.

An implicit time integration algorithm based on a linearized second-order Euler backward difference is used to advance the solution in time. Initially, a steady-state solution is obtained for a fixed rotor position based on local time stepping. Then the time-accurate calculation is performed using the converged steady-state solution as the

initial condition. Dual-time stepping is also adopted to improve the solution accuracy if necessary. The linear system of equations is solved at each time step using a point Gauss-Seidel method.

At the far-field boundary, the pressure is fixed to the free stream value and other flow variables are extrapolated from the interior. The far-field boundary is located seven radii away from the rotor.

For the effective treatment of the complicated flow field involving the relative motion between the blades and the fuselage, the computational domain is decomposed into two zones. The upper zone contains the rotor blades and rotates with them. The stationary lower zone covers the rest of the flow field including the fuselage and the far wake of the rotor. The computational grid of each zone is constructed independently, and a sliding grid algorithm is applied to the boundary between the two zones such that the flow variables convect across the boundary in a conservative manner[8,9]. The flux at each boundary face is calculated by using the information about the overlapping area between the upper and lower sliding boundary faces. The second-order spatial accuracy of the flux discretization is maintained across the sliding boundary by introducing ghost cells attached to the sliding boundary faces inside the opposite flow zone.

To reduce the numerical dissipation and to enhance the tip-vortex preservation, solution-adaptive grid refinement can be used. A 'quasi-unsteady' grid adaptation technique is adopted to maintain a proper grid resolution, while avoiding excessive computational time required for the dynamic grid adaptation applied in a fully unsteady manner.

The unsteady flow for unstructured grid is calculated by advancing the rotor by 0.5 degrees at each time step. The calculation is made using 28 and 8 processors for the upper and lower zones, respectively, and it takes approximately six hours of elapsed CPU time for one rotor revolution on the refined grid. Dual-time stepping is not adopted in the present calculation.

All calculations are performed on a Linux-based PC cluster having 2.4Ghz Pentium IV CPUs.

2.3 ROTOR TRIM

In order to attain the calculated thrust to a desired level and to eliminate the rotor aerodynamic moment, a rotor trim procedure is enforced for rotors in forward flight for unstructured grid calculations. The thrust and moment coefficients can be expressed as a function of the collective angle, θ_0 and cyclic pitch angles, θ_{1C}, θ_{1S} as shown in the following equation.

$$\theta = \theta_0 - \theta_{1C}\cos\psi - \theta_{1S}\sin\psi$$

Then the equilibrium state is obtained by correcting the trim angles iteratively using the Newton-Raphson method[8,10]. In this process, the correction angles of the control settings are estimated by evaluating the sensitivities which are the derivatives of the thrust and the pitching and rolling moments with respect to the control angles. Each trim cycle consists of seven revolutions of the rotor, three for calculating the sensitivities and the rest for the solution iteration. This trim procedure is computationally very expensive since it requires several cycles for a converged solution. Initially, the rotor trim iteration is performed on the coarse grid. Once the trim cycle is converged, the grid adaptation is applied to the coarse grid, and then the rotor trim procedure is continued to obtain the final trim solution on the refined grid.

For structured grid calculation, a trim data is given as an input data, and these trim conditions are shown in Table 1.

Table 1: Trim conditions of ROBIN model used for calculations

Trim Conditions		KAIST	JAXA
Advanced ratio		0.23	
Tip Mach number		0.5298	
Thrust coefficient, *CT*		0.006484	0.006549
Pitch angle at 70% of rotor span (θ)	Collective angle	6.6	6.47
	Cyclic (longitudinal)	-3.61	-2.08
	Cyclic (lateral)	1.54	3.28
	Phase lag	0	0
Flapping angle	B0	0	
	BC	0	
	BS	0	
Rotor shaft angle		3	
Rotation of fuselage	Roll	0	
	Pitch	0	

3. GRID GENERATION

3.1 ROBIN Configuration

The ROBIN configuration, which is tested at NASA Langley (Refs. 1-3), is consists of a four-bladed rotor and a generic fuselage. The blades are made of an NACA0012 airfoil section and have a rectangular planform shape with an aspect ratio of 12.98. The blades are linearly twisted by -8 degrees from root to tip and have a root cutout of 0.24R. The shaft is tilted forward by 3 degrees. Figure 1 shows photographs of the 2-meter ROBIN configuration installed in the 14- by 22-foot subsonic tunnel test section, which was used for the experiment of Ref. 3.

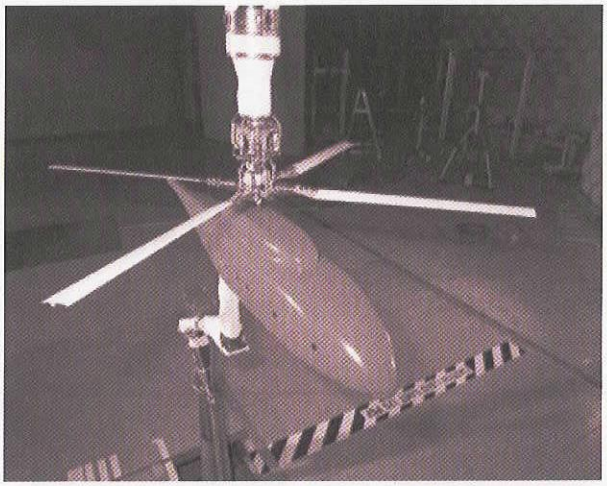

L97-03935

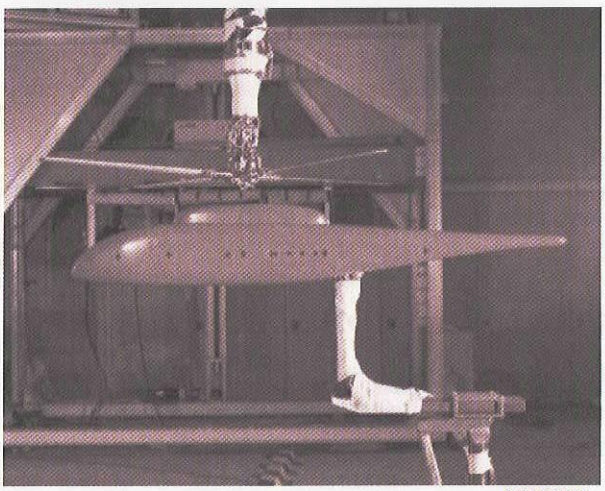

L97-03936

Figure 1: Photographs of the 2-meter ROBIN configuration installed in the 14- by 22-Foot Subsonic Tunnel test section[3]

Figure 2 and Table 2 show the sketch of the ROBIN configuration and coefficients to define the body shape of ROBIN configuration, which are used in the related equations.

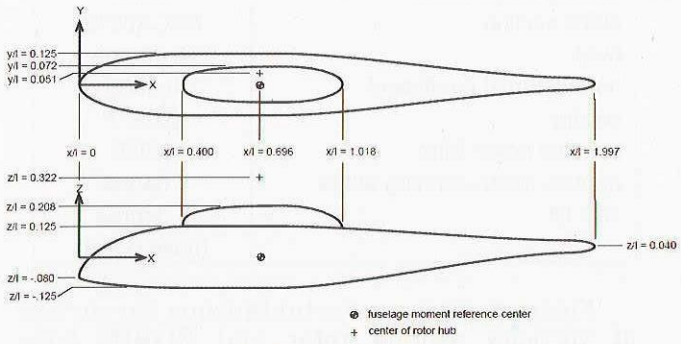

Figure 2: Sketch of the ROBIN configuration

Table 2: Coefficients to define body shape of ROBIN configuration and related equations[1]

Coefficients to Define Body Shape

Function	C_1	C_2	C_3	C_4	C_5	C_6	C_7	C_8
	$0.0 < x/l < 0.4$							
H	1.0	-1.0	-.4	.4	1.8	0.0	.25	1.8
W	1.0	-1.0	-.4	.4	2.0	0.0	.25	2.0
Z_0	1.0	-1.0	-.4	.4	1.8	-.08	.08	1.8
N	2.0	3.0	0.0	.4	1.0	0.0	1.0	1.0
	$0.4 < x/l < 0.8$							
	C_1	C_2	C_3	C_4	C_5	C_6	C_7	C_8
H	.25	0.0	0.0	0.0	0.0	0.0	0.0	0.0
W	.25	0.0	0.0	0.0	0.0	0.0	0.0	0.0
$Z0$	0.0	0.0	0.0	0.0	0.0	0.0	0.0	0.0
N	5.0	0.0	0.0	0.0	0.0	0.0	0.0	0.0

$$\begin{bmatrix} H(x/l) \\ W(x/l) \\ Z_0(x/l) \\ N(x/l) \end{bmatrix} = C_6 + C_7\left(C_1 + C_2\left(\frac{x/l + C_3}{C_4}\right)^{C_5}\right)^{1/C_8}$$

$$r = \left(\frac{\left(\frac{H}{2}\frac{W}{2}\right)^N}{\left(\frac{H}{2}\sin\varphi\right)^N + \left(\frac{W}{2}\cos\varphi\right)^N}\right)^{1/N} \qquad \begin{aligned} y/l &= r\sin\varphi \\ z/l &= r\cos\varphi + Z_0 \end{aligned}$$

3.2 Surface & Background Grid Generation

For the structured grid, 131×100×30 nodes for ROBIN body and 129×101×30 nodes for blades are used. And the inner background grids is 290×230×80 and the outer background grids is 83×79×49 nodes.

For the unstructured grid, 3,247,740 and 1,030,250 cells are generated for the rotating and stationary zones respectively after two levels of grid adaptation. The sliding boundary plane is set at 1.66 chord lengths underneath the rotor disk plane.

Table 3: Grid number for structure grid

Grid	
Inner Background grid	**(x×y×z) 450×400×80 = 14,400,000**
Outer Background grid	**(x×y×z) 83×79×49 = 321,293**
Main-rotor grid	**(chord×normal×span)×blade (127×30×131)×4 = 1,996,440**
Fuselage grid	**(chord×normal×span)×blade 131×30×126 = 495,180**
Total	**17,212,913 points**
Spacing of inner background Grid	**$0.1c(=0.005R)$**

Table 4: Grid number for unstructure grid

	Initial grid	After two level grid adaptation
Rotating zone	646,452	3,247,740
Stationary zone	428,831	1,030,250

Table 3 and 4 show the specification of structured and unstructured grid used for calculation.

Figure 3 shows the computational surfaces on ROBIN surface for unstructured and structured grid respectively, and Figure 4(a)-(d) shows several computational grids of background grid on the rotor-fuselage configuration for each grid type. As explained in the previous section, the structured grid is a moving overlapped grid system as shown in Fig. 4(b). It is composed of main-rotor blade grids, tail-rotor blade grids, fuselage grid, inner background grid, and outer background grid. For unstructured grid, the computational domain is decomposed into two zones, the upper rotating zone with rotor blades and the lower stationary zone with the fuselage.

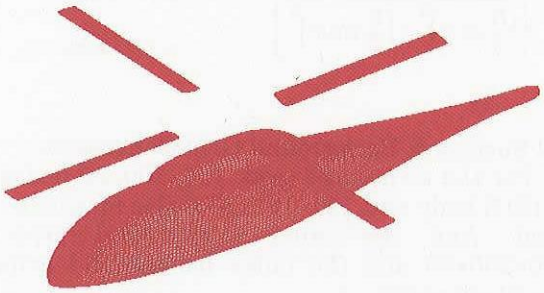

(a) structured overset grid

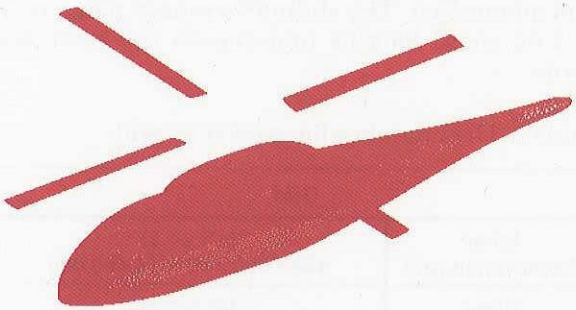

(b) unstructured sliding grid

Fig.3: Computational surfaces for the ROBIN configuration

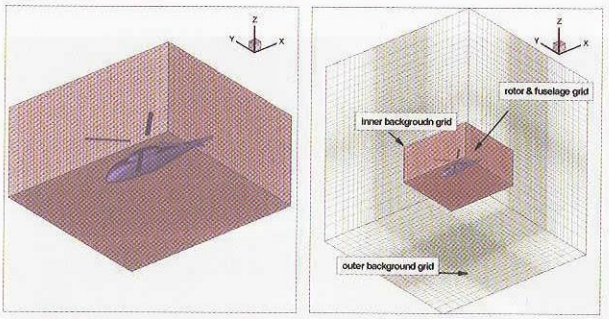

(a) rotor/fuselage grids (b) whole overlapped grid

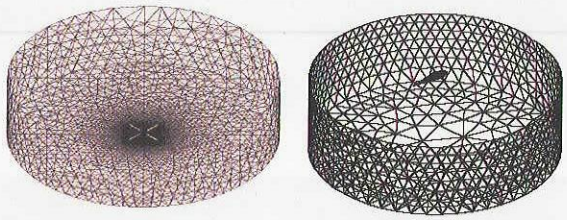

(c) upper rotating zone (d) lower stationary zone

Fig.4 Computational grid for the rotor-fuselage configuration; structured overset grid (a, b) and unstructured sliding grid (c, d)

4. CALCULATION RESULTS

Among the various measurement cases reported from the experiment, the one with a blade tip Mach number of 0.52 and an advance ratio of 0.23 is chosen for validation. Table 5 shows the operating conditions and parameters used in the calculations.

Table 5: Operating conditions and parameters

Property	Value
blade planform	Rectangular
radius	0.8606 m
root chord	0.0660 m
tip chord	0.0660 m
number of blades	4
root cutout location	0.24R
flap/lag hinge location	0.06R
airfoil section	NACA0012
twist	-8 degree
normal thrust coefficient	0.0065
solidity	0.0977
nominal hover Mttp	0.055
approx. mean conning anlge	1 degree
shift tilt	3 degree (nose down)

Figure 5 shows an instantaneous iso-surface of vorticity around rotor and ROBIN body configuration using structured grid. Tip-vortices generated from 4 blades are well

demonstrated, and the ROBIN body is also well captured.

In Fig. 6, the predicted unsteady pressure variations of both structured and unstructured grids are compared with the experiment at four selected fuselage surface points. Along the top line of the fuselage, the peak-to-peak magnitude of the variation and the phase are well predicted, even though the predicted result is slightly higher than the experiment at the point ahead of the pylon. At the side surface of the fuselage, the magnitude of the predicted pressure is consistently higher than the experiment. A similar result is also obtained at the retreating side. Both CFD codes of JAXA and KAIST show good agreement with experimental data.

In Fig. 7, the instantaneous vorticity contours at the fuselage symmetric plane are presented for four azimuth angles of the blade for comparison. The figures demonstrate the generation and the migration of the tip vortex for several revolutions. At this relatively high advance ratio, the direct impingement of the tip vortex on the fuselage is not observed, even though the downwash and the pressure on the fuselage are strongly affected by the blade passage as confirmed in the previous figures. Even both results show good agreement in the trace of tip vortex, results of structured grid show more distinct tip vortex in vortex capturing ability. One of the reasons comes from the usage of finer grid and higher-order scheme in the wake-capturing region by using overlapped grid.

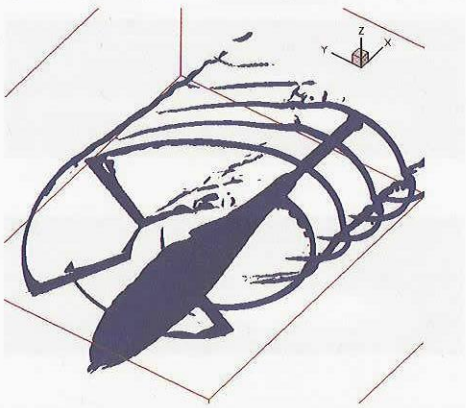

Figure 5: Instantaneous iso-surface of vorticity around rotor and ROBIN configuration

5. SUMMARIES AND CONCLUSIONS

Three dimensional parallel Euler flow solvers have been developed for the simulation of unsteady rotor-fuselage interaction aerodynamics on both structured and unstructured grids using the ROBIN (ROtor Body INteraction) configuration.

(1) Both CFD codes of JAXA and KAIST show good agreement with experimental data.
(2) Results of JAXA show excellence in vortex capturing ability, but need to use better trim condition for better agreement with experimental data.
(3) Results of KAIST show excellence in speedy trim calculation, but need to increase solution accuracy for better tip vortex capturing.
(4) During cooperative research work, each institute can clearly understand the weak point of each CFD code to make up for the better results.

6. REFERENCES

[1] Raymond, E.M., and Gorton, S.A., "Steady and Periodic Pressure Measurements on a Generic Helicopter Fuselage Model in the Presence of a Rotor," NASA TM 2000-210286, 2000.

[2] Elliot, J.W., Altoff, S.L., and Sailey, R.H., "Inflow Measurement Made with a Laser Velocimeter on a Helicopter Model in Forward Flight, Volume II, Rectangular Planform Blades at an Advance Ratio of 0.23," NASA TM 100542, 1988.

[3] Boyd, Jr., D.D., Barnwell, R.W., and Gorton, S.A., "A Computational Model for Rotor-Fuselage Interactional Aerodynamics," AIAA Paper 2000-0256, 2000.

[4] Roe, P. L., "Approximate Riemann Solvers, Parameter Vectors and Difference Schemes," Journal of Computational Physics, Vol. 43, (2), pp. 357-372, 1981.

[5] Aoyama, T., Kawachi, K., Saito, S., "Unsteady Calculation for Flow-field of Helicopter Rotor with Various Tip Shapes," 18th European Rotorcraft Forum, Paper No.B03, Avignon, France, September, 1992.

[6] Yamamoto, S. and Daiguji, H., Higher-Order-Accurate Upwind Schemes for Solving the Compressible Euler and Navier-Stokes Equations, J. of Computers & Fluids, 22, pp.259-270, 1993.

[7] Shima, E. and Jounouchi, T., Role of CFD in Aeronautical Engineering (No.14) - AUSM type Upwind Schemes -, NAL SP-34, pp.7-12, 1999.

[8] Park, Y. M., and Kwon, O. J., "Simulation of Unsteady Rotor Flow Fields Using Unstructured Sliding Meshes," Journal of the American Helicopter Society, Vol. 49, (4), pp.391-400, 2004.

[9] Thomas, P. D., and Lombard, C. K., "Geometric Conservation Law and Its Application to Flow Computations on Moving Grids," AIAA Journal, Vol. 17, (10), pp.1030-1037, 1979.

[10] Yang, Z., Sankar, L. N., Smith, M., and Bauchau, O., "Recent Improvement to a Hybrid Method for Rotors in Forward Flight," AIAA Paper 2000-0260, 2000.

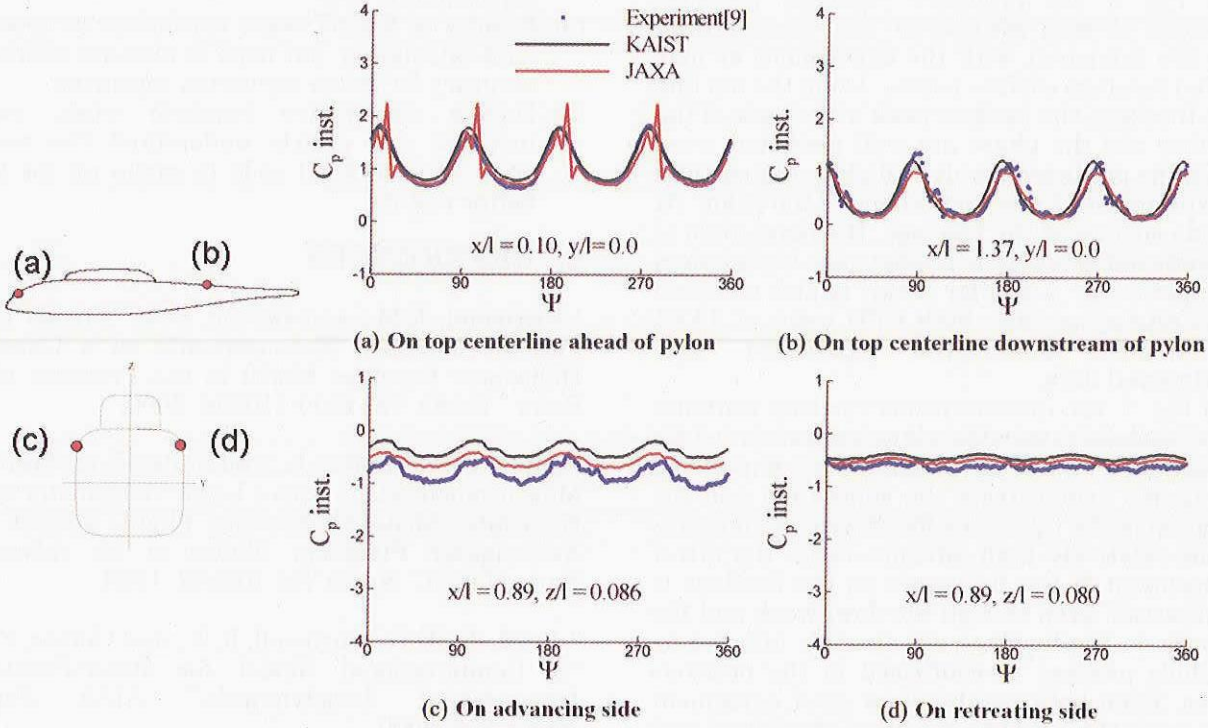

Figure 6: Comparison of predicted unsteady pressure variations at four selected fuselage surface points

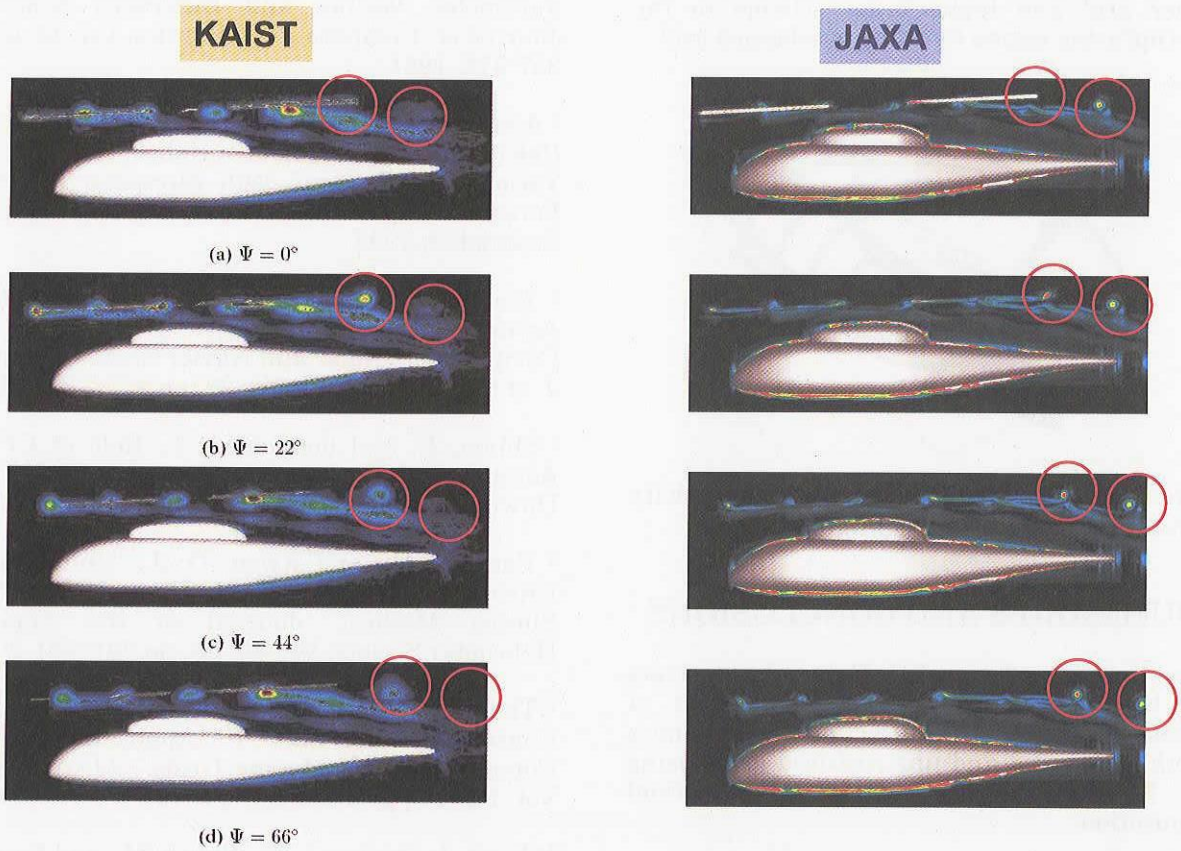

Figure 7: Comparison of instantaneous vorticity contours at the fuselage symmetric plane